

# Statistical cerebrovascular segmentation in three-dimensional rotational angiography based on maximum intensity projections

Rui Gan,<sup>a)</sup> Wilbur C. K. Wong,<sup>b)</sup> and Albert C. S. Chung<sup>c)</sup>

*Lo Kwee-Seong Medical Image Analysis Laboratory,*

*Department of Computer Science,*

*The Hong Kong University of Science and Technology, Hong Kong*

(Received 22 December 2004; revised 7 June 2005; accepted for publication 23 June 2005; published 30 August 2005)

Segmentation of three-dimensional rotational angiography (3D-RA) can provide quantitative 3D morphological information of vasculature. The expectation maximization (EM)-based segmentation techniques have been widely used in the medical image processing community, because of the implementation simplicity, and computational efficiency of the approach. In a brain 3D-RA, vascular regions usually occupy a very small proportion (around 1%) inside an entire image volume. This severe imbalance between the intensity distributions of vessels and background can lead to inaccurate statistical modeling in the EM-based segmentation methods, and thus adversely affect the segmentation quality for 3D-RA. In this paper we present a new method for the extraction of vasculature in 3D-RA images. The new method is fully automatic and computationally efficient. As compared with the original 3D-RA volume, there is a larger proportion (around 20%) of vessels in its corresponding maximum intensity projection (MIP) image. The proposed method exploits this property to increase the accuracy of statistical modeling with the EM algorithm. The algorithm takes an iterative approach to compiling the 3D vascular segmentation progressively with the segmentation of MIP images along the three principal axes, and use a winner-takes-all strategy to combine the results obtained along individual axes. Experimental results on 12 3D-RA clinical datasets indicate that the segmentations obtained by the new method exhibit a high degree of agreement to the ground truth segmentations and are comparable to those produced by the manual optimal global thresholding method. © 2005 American Association of Physicists in Medicine. [DOI: 10.1118/1.2001820]

Key words: Image segmentation, 3D rotational angiography (3D-RA), maximum intensity projection (MIP), expectation maximization (EM) algorithm, finite mixture model (FMM)

## I. INTRODUCTION

An accurate description of the cerebrovascular tree is important to clinical diagnosis and quantitative analysis of the vascular diseases. Based on the segmentation of the vascular tree, a patient-specific three-dimensional (3D) vascular model can be very useful to surgical planning. There are various methods proposed for the segmentation of vessels. For instance, model-based techniques explicitly modeling vessel segments as tubular objects have been developed for the segmentation of angiograms.<sup>1-3</sup> Geodesic active contours and level sets methods have been used for the segmentation of vasculature in magnetic resonance angiography (MRA).<sup>4,5</sup> Alternatively, a 3D region growing algorithm has been introduced for segmenting vasculature in time-of-flight (TOF) MRA.<sup>6</sup> Furthermore, statistical segmentation methods based on the expectation maximization (EM) algorithm have been devised for extracting vessels in TOF-MRA<sup>7-9</sup> and phase contrast (PC) MRA.<sup>10-12</sup>

3D rotational angiography (3D-RA) is a relatively new imaging technique in neuroradiological interventions.<sup>13-16</sup> It can provide morphological information of the cerebral vessels during operations and is a very useful imaging tool for assessing intracranial aneurysms, stenoses, and arteriovenous malformations (AVM) in endovascular treatments.

The global thresholding method is a practical and efficient approach to 3D-RA vascular segmentation. Threshold-based segmentations have been adopted in the evaluation of diffusion techniques in 3D-RA images.<sup>17</sup> As vessels are enhanced by the use of a contrast agent, according to radiologists' feedback, the segmentation of 3D-RA with a global threshold is good enough for most of the clinical applications. Owing to the relatively large variance in intensity values of vessels among different images, it is apparently impossible to yield satisfactory segmentations if a single predefined threshold is used to segment all 3D-RA images. As such, for each image, it is necessary for a radiologist to select the global threshold manually in order to produce adequate segmentation. The manual threshold selection process can be very subjective among different radiologists and it is of low reproducibility. Therefore, an automatic threshold selection method is preferable in practice.

The finite mixture model (FMM) and the EM algorithm, with the maximum likelihood (ML) estimation, provide computationally efficient means for the automatic global threshold selection. By working along the same line as Wilson *et al.*,<sup>8</sup> a double-Gaussian mixture model can be adopted to estimate the intensity distribution of 3D-RA images consisting of vessel (high-intensity values) and background classes.

It is observed that the volume occupied by vessels typically is very small (on average, around 1% of the total volume) in clinical 3D-RA datasets. Such a severe imbalance between the proportions of two classes makes it difficult to accurately model the intensity distribution of 3D-RA images. The Gaussian distribution corresponding to vessels may shift to the low-intensity range as a result of the EM algorithm. Hence, a relatively low threshold is selected and 3D-RA images are oversegmented.

To deal with this problem, based on our prior work,<sup>18</sup> a new approach is proposed to segment vasculature in 3D-RA images. The method is also based on FMM and the EM algorithm. But, the aforementioned problem in modeling the imbalanced intensity distribution of 3D-RA images is ameliorated with the use of maximum intensity projection (MIP) images. The method exploits a useful property of MIP, i.e., the proportion of vessels in the MIP image is larger than that in the original 3D volume, to increase the stability in the parameter estimation of FMM with the EM algorithm. It takes an iterative approach to segmenting 3D-RA images progressively with the segmentation of MIP images along the three principal axes, and uses a winner-takes-all strategy to combine the results obtained along individual axes. The method is fully automatic and computationally efficient.

The proposed method has been tested on 12 clinical 3D-RA datasets. The results indicate that the segmentations obtained by the method exhibit a high degree of agreement to the manual segmentations (which are treated as the ground truth). In a further comparison, it is found that the segmentation from the new algorithm is comparable to the one produced by the global thresholding method with the manual optimal threshold. Note that the manual optimal threshold is an intensity value that gives segmentation in maximum agreement to the ground truth, i.e., it can be found only if the ground truth is known in advance.

## II. AUTOMATIC GLOBAL THRESHOLD SELECTION WITH FMM AND THE EM ALGORITHM

The finite mixture model (FMM) and the expectation maximization (EM) algorithm have been employed to segment medical images with the maximum likelihood (ML) estimation. This approach is known as the EM-based segmentation method (hereafter referred to as auto-GT, i.e., automatic global thresholding). It has been widely used in the medical image processing community<sup>7-10,12,19,20</sup> because of its simplicity and computational efficiency.

Auto-GT assumes that the image pixel or voxel intensity values are independent and identically distributed (i.i.d.), and the distribution of the observed intensity values can be approximated by a FMM. The method can be summarized as follows: (1) statistical modeling with the FMM, (2) parameter estimation of FMM, and (3) global threshold selection based on the ML criterion and the prior knowledge on the intensity distribution.

FMM is a flexible and powerful probabilistic modeling tool for univariate and multivariate data. In this paper, the intensity distribution of 3D-RA images is approximated by a

mixture of Gaussian distributions. Therefore, the distribution of the voxel intensity values can be expressed as follows:

$$p(i) = \sum_{k=1}^M \omega_k f(i|k), \quad (1)$$

where  $i$  represents the intensity value,  $p(i)$  is the probability (i.e., normalized frequency) of the intensity  $i$ ,  $M$  is the number of distributions in the mixture model,  $f(i|k)$  is a distribution function representing the likelihood probability of the intensity  $i$  given the distribution  $k$ , and  $\omega_k$  is a positive weight representing the prior probability of the distribution  $k$ . It is noted that  $\sum_k f(i|k) = 1$ ,  $0 \leq \omega_k \leq 1$  ( $\forall k \in \{1, \dots, M\}$ ) and  $\sum_{k=1}^M \omega_k = 1$ .

The parameters of FMM in Eq. (1) are then estimated by the EM algorithm. The algorithm takes an iterative approach to estimating the parameters by maximizing the log likelihood of the mixture model.<sup>21</sup> At each iteration, the EM algorithm performs the following two steps: (1) E step and (2) M step. Let  $\Phi$  be the set of parameters in Eq. (1),  $\mathcal{I}$  be the set of intensity values in the image, and  $\mathcal{X}$  be the set of labels for all the distributions in the mixture model. The two steps of the EM algorithm can be mathematically presented as follows: given the initial estimation  $\Phi^{(0)}$ , at the  $t$ th iteration:

*E step:* calculate the conditional expectations,

$$Q(\Phi|\Phi^{(t)}) = E[\log p(\mathcal{X}, \mathcal{I}|\Phi)|\mathcal{I}, \Phi^{(t)}]; \quad (2)$$

*M step:* maximize  $Q(\Phi|\Phi^{(t)})$  to derive  $\Phi^{(t+1)}$ ,

$$\Phi^{(t+1)} = \arg \max_{\Phi} Q(\Phi|\Phi^{(t)}). \quad (3)$$

The algorithm terminates if the changes in the log likelihood and parameters are sufficiently small.

Finally, the global threshold is selected based on the prior knowledge on the intensity distribution and the ML estimation. Suppose it is known that the intensity distribution of vessels in 3D-RA images is modeled by the distribution  $k = M$ , the vessels can be segmented with the ML estimation.<sup>21</sup> In other words, a voxel is classified as vessel if the voxel intensity value,  $i$  satisfies

$$\omega_M f(i|M) > \sum_{j=1}^{M-1} \omega_j f(i|j). \quad (4)$$

Because the positive weights  $\omega_k$  ( $k \in \{1, \dots, M\}$ ) are constant, a global threshold  $T$  for segmenting vessels in a 3D-RA image can be obtained by calculating the intersection of  $\omega_M f(i|M)$  and the rest of the distributions in the mixture model, i.e.,  $\sum_{j=1}^{M-1} \omega_j f(i|j)$ .

## III. STATISTICAL MODELING OF INTENSITY VALUES IN 3D-RA IMAGES

To the best of our knowledge, a theoretical study on statistical modeling for PC-MRA was conducted,<sup>10,22</sup> while there is no work on statistical analysis of the intensity distribution for TOF-MRA and 3D-RA. Nevertheless, in the EM-based segmentation algorithm for TOF-MRA presented by Wilson *et al.*,<sup>8</sup> it is assumed that each intensity class has a

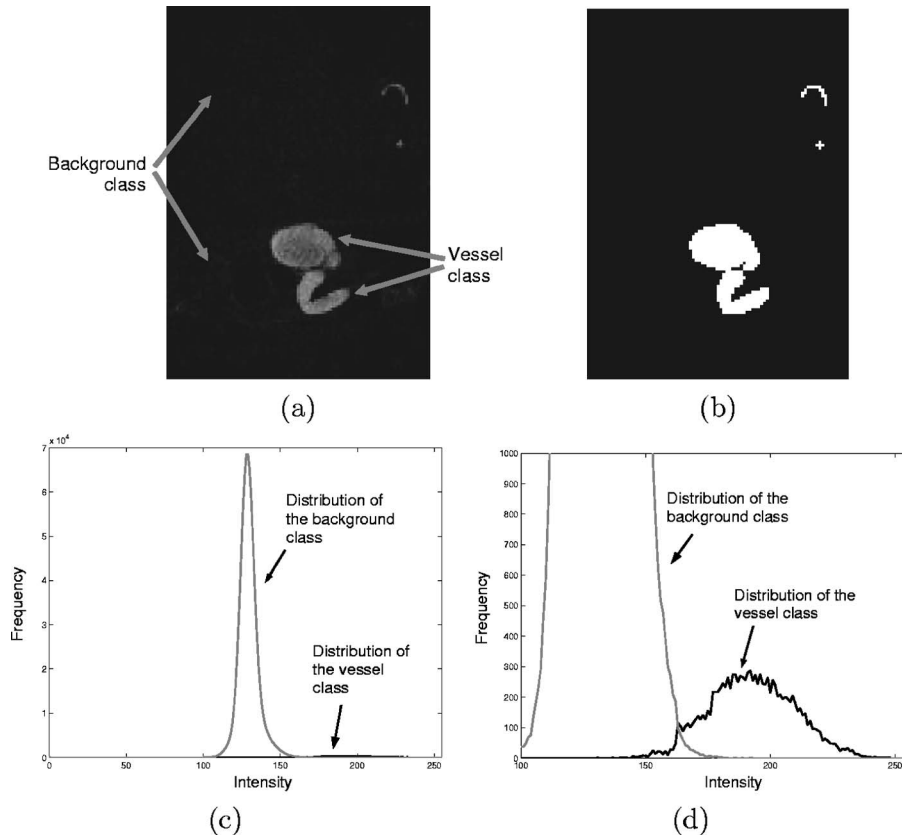


FIG. 1. (a) A slice of a typical 3D-RA dataset. (b) Manual segmentation. (c) The intensity distributions of the vessel and background volumes in the dataset. (d) A close-up.

Gaussian distribution of intensities. In this section, a similar empirical study on statistical modeling of the intensity values in 3D-RA images is presented.

Vessels in 3D-RA images are usually bright or in high intensity values. Figure 1(a) shows a slice image of a typical 3D-RA dataset. With the help of a consultant radiologist, the vascular structures are segmented manually, and Fig. 1(b) shows the manual segmentation. Figure 1(c) shows the intensity distributions, which are estimated based on the manual segmentation, of the nonvessel (aka background) and vessel volumes in the dataset. A close-up on the right tail of the intensity distribution of the background volume is shown in Fig. 1(d) for a better illustration of the vessel intensity distribution. It is evident that the intensity values of vessels are, in general, higher than those of the background. Similar to Wilson *et al.*,<sup>8</sup> the intensity distribution of vessels in 3D-RA images is approximated by a Gaussian distribution with a higher mean, while that of the background is modeled by a Gaussian distribution with a lower mean. In other words, the observed intensity distribution of a 3D-RA image can be approximated by a double-Gaussian mixture model as follows:

$$p(i) = \sum_{k=1}^2 \omega_k \frac{1}{\sqrt{2\pi\sigma_k^2}} \exp\left[-\frac{(i - \mu_k)^2}{2\sigma_k^2}\right], \quad (5)$$

where  $\mu_1$  and  $\mu_2$  ( $\mu_1 < \mu_2$ ) are the means, and  $\sigma_1$  and  $\sigma_2$  are

the standard deviations of the two Gaussian distributions, respectively.

In the experiments on 12 3D-RA datasets, it is observed that the segmentations produced by auto-GT are less than satisfactory (see Sec. V C for more details). The 3D-RA images are oversegmented with relatively low thresholds. A low threshold is selected in auto-GT because the volume occupied by vessels in a 3D-RA dataset is too small, as compared with the background volume. It is found that, among the 12 clinical datasets, the proportion of vessels in the 3D-RA image, which is computed based on manual segmentations, is around 1%. The large difference between sample sizes of background and vessels introduces great difficulty to the EM algorithm in accurately estimating the parameters of the double-Gaussian mixture model. It is a well-known and practical problem that the EM algorithm would be biased against small structures that just occupy a very small portion, when a severe imbalance exists between the proportions of different intensity classes. Owing to the fact that there are very few voxels in high-intensity values, the Gaussian distribution with a higher mean may shift to the low-intensity range (left) in the parameter estimation process, as illustrated in Fig. 2. Figure 2(a) shows the estimated Gaussian distributions (solid lines) for approximating the observed intensity distribution of the aforesaid 3D-RA dataset in Fig. 1 [dotted lines plot the

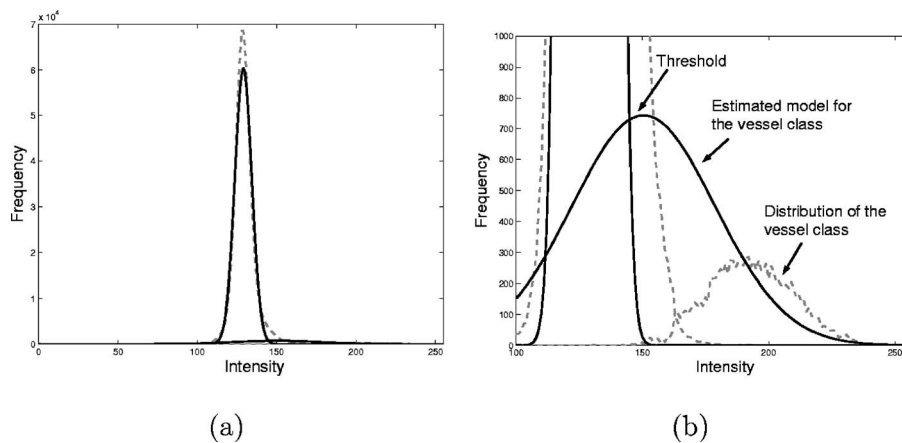


FIG. 2. (a) The estimated Gaussian distributions (solid lines) for approximating the intensity distributions (dotted lines) of the dataset presented in Fig. 1. (b) A close-up.

same distributions as in Fig. 1(c)]. Figure 2(b) shows the close-up on the right tail of the Gaussian distribution with a lower mean.

In order to improve the parameter estimation of FMM with the EM algorithm, we suggest that the parameters of FMM should not be estimated with the whole 3D volume. Instead, the parameter estimation is performed with maximum intensity projection (MIP) images of the volume. MIP is the simplest volume rendering technique and is commonly used to visualize 3D vascular morphology on 2D image (i.e., the MIP image).<sup>23,24</sup> The MIP image is a 2D projection of a 3D volume, where the intensity value assigned to a pixel is the highest one found in the 3D volume along the projection line. Because of the nature of the MIP image formation, it is an effective visualization tool if the objects of interest are brighter than the unwanted structures in the volume. This results in an ideal application of MIP in visualizing angiographies such as MRA,<sup>25</sup> contrast-enhanced (CE) computed tomography angiography (CTA)<sup>26</sup> and 3D-RA. Recently, MIP is also used in a preprocessing step of a vascular segmentation method for TOF-MRA,<sup>6</sup> which exploits the MIP depth  $Z$  buffer to generate seed points for further 3D region growing segmentation.

In this paper, a property of MIP, i.e., the proportion of vessels in the MIP image is larger than that in the original 3D volume, is exploited to estimate the parameters of FMM more robustly. Figure 3(a) shows one axial MIP image of the dataset presented in Fig. 1. Figure 3(b) plots the intensity distributions of the vessel and background volumes, which are determined with reference to a manual segmentation. It is observed that, among the 12 clinical datasets, the proportion of vessels in an axial MIP image is around 20%. This proportion is much greater than that in 3D volume, which is around 1%.

Without loss of generality, a double-Gaussian mixture model is adopted to approximate the MIP image intensity distribution. Figure 3(c) shows the estimated Gaussian distributions (solid lines) for the observed intensity distributions presented in Fig. 3(b). Note that the Gaussian distribution with a higher mean approximates the vessel intensity distri-

bution better than the estimation shown in Fig. 2(b), where the Gaussian function is shifted to the low-intensity range. Because of the increase in the proportion of vessels in MIP images, the intensity distribution of vessels can be approximated more accurately. Further experimental results are given in Sec. V A to justify this proposition.

Based on the estimated statistical model of MIP image intensity distribution, a global threshold for segmentation can be selected with the ML estimation. But, the thresholds for segmenting MIP images are not adequate for globally thresholding original 3D volumes. It is found that the difference between the threshold for segmenting a MIP image and the optimal threshold for segmenting the original 3D volume varies significantly among different datasets. The optimal threshold is an intensity value that can produce segmentation with the global thresholding method, in maximum agreement to the ground truth. As such, the 3D volume can be either oversegmented or undersegmented if one uses the threshold estimated from the MIP image intensity distribution for the segmentation.

One may intend to compute a 3D bounding box or a local 3D region of interest (ROI) based on a rough segmentation of the vascular structures (for instance, heuristic global thresholding) to alleviate the large difference between sample sizes of the background and vessels, which may make the EM algorithm provide more accurate estimates on the parameters of the double-Gaussian mixture model. However, some difficulties exist. First, some vessels may not be included in the rough segmentation due to the variation of intensity values inside vasculature. As such, it cannot guarantee that a 3D bounding box would cover the whole vasculature. Second, the vessel voxels in the preliminary segmentation can be scattered over the 3D space. Therefore, it is apparently impossible to compute a 3D ROI locally with respect to the vasculature. Finally, the vasculature commonly spreads very widely in the volume and, as a result, computing a 3D bounding box may not obviously reduce the proportion difference among the two classes.

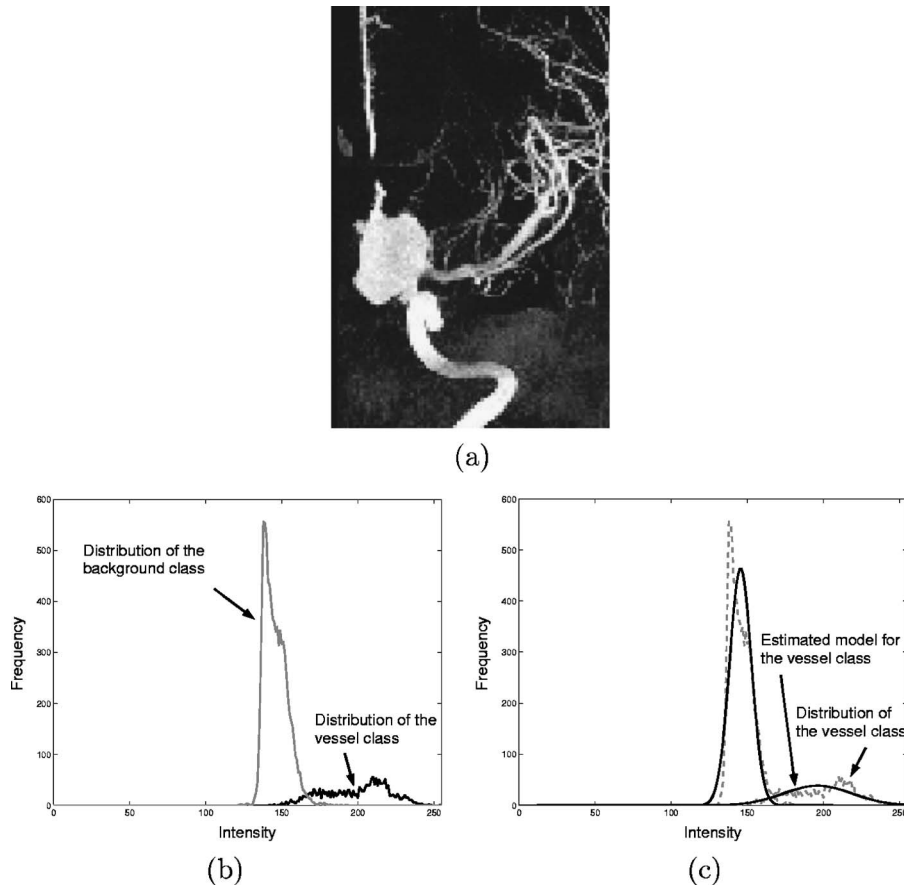


FIG. 3. (a) One axial MIP image of the dataset shown in Fig. 1. (b) The intensity distributions of the two classes. (c) The estimated Gaussian distributions (solid lines).

#### IV. NOVEL SEGMENTATION TECHNIQUE USING MIP IMAGES

In Sec. IV A we outline the new technique for segmenting 3D-RA vascular structures. The method compiles the vascular segmentation iteratively through the segmentation of MIP images projected along a fixed direction. The iterative process is terminated automatically based on a stopping criterion discussed in Sec. IV B. A proper extension of the algorithm to exploit the segmentations of MIP images projected along multiple directions is presented in Sec. IV C. This extension is proposed for the robustness of the algorithm.

##### A. Outline of the method

The method begins with generating a MIP image from the original 3D volume. To avoid unnecessary intensity interpolation, the projection direction is set to one of the three principal and orthogonal axes. The MIP image is then segmented by the EM-based segmentation method (see Sec. II). A double-Gaussian mixture model is used for approximating the intensity distribution of the MIP image, as discussed at the end of Sec. III.

At each iteration, the 3D vascular segmentation is achieved progressively based on the segmentation of the MIP images. During the MIP image generation, the 3D position of the voxels that contributed to the MIP image (i.e.,

voxels with their intensity values projected onto the MIP image) is recorded. The voxels corresponding to vessel pixels, which are classified as vessel in the MIP image with the EM-based segmentation method, are included in the 3D vascular segmentation. Those voxels are then removed from the 3D volume and will not contribute to the MIP image generation at the next iteration.

A new MIP image is generated from the 3D volume (with the exclusion of voxels counted on the 3D vascular segmentation) at the successive iterations. Following the segmentation of the new MIP image, the voxels corresponding to vessel pixels in the MIP image are added to the 3D vascular segmentation, as mentioned in the previous paragraph. The algorithm continues to iterate until no pixels are classified as a vessel in the MIP image.

It is noted that, at each successive iteration, more vessel voxels are added to the 3D vascular segmentation and excluded in the maximum intensity projection process. Due to the significant decrease in the number of high-intensity pixels (i.e., the number of vascular pixels) in the subsequent MIPs, as pointed out in Sec. III, the Gaussian distribution with a higher mean in the mixture model may shift to the lower-intensity region. A relatively low threshold is then selected to segment the MIP image and, as a result, oversegmentation is produced. Therefore, a stopping criterion is proposed for the iterative algorithm to detect the left-shift of the

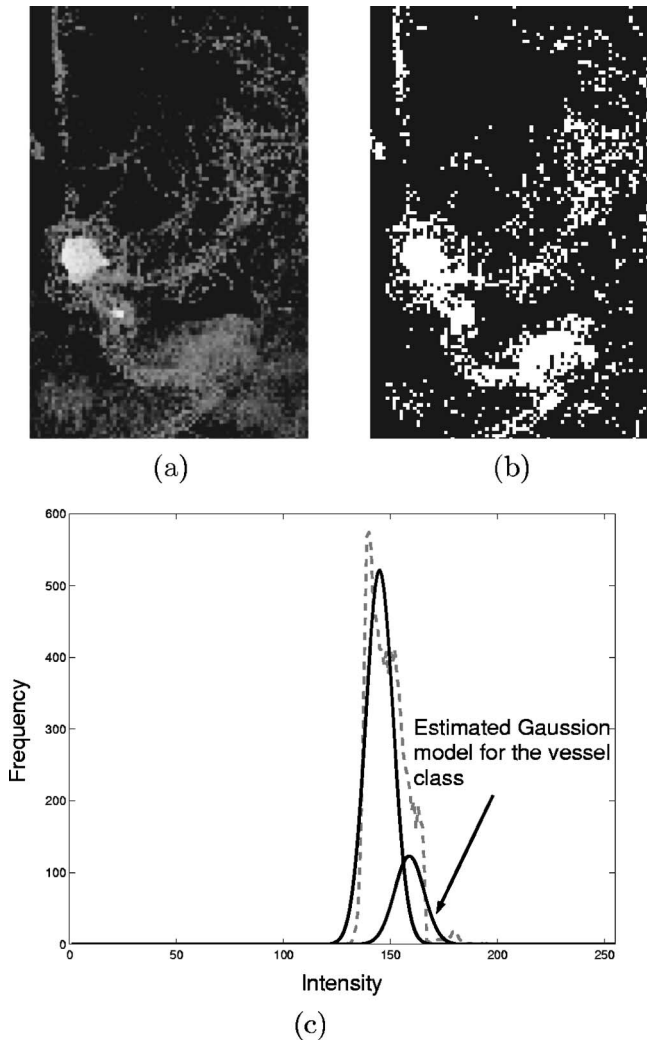


FIG. 4. (a) The axial MIP image at the 16th iteration. (b) The obtained segmentation. (c) The estimated Gaussian distributions (solid lines) and the observed intensity distribution (dotted line).

aforsaid Gaussian distribution and the termination of the algorithm. The stopping criterion is presented in Sec. IV B.

The algorithm is implemented separately along three principal axes. Segmentation results along individual axes are then fused using a winner-takes-all strategy, which is presented in Sec. IV C.

## B. Stopping criterion

The intensity distribution of the MIP image is evolving across iterations. The number of high-intensity pixels decreases as the algorithm proceeds. Figure 4(a) shows the axial MIP image generated at the 16th iteration in the execution of the iterative segmentation method on the same 3D-RA dataset presented in Fig. 3. The white spot on the middle left-hand side in Fig. 4(a) indicates the presence of vessels. Figure 4(b) shows the segmentation obtained by the EM-based segmentation method. Figure 4(c) plots the estimated Gaussian distributions (solid lines) and the observed intensity distribution (dotted line) of the MIP image. It is observed that, in Fig. 4(c), the number of pixels in the

higher-intensity range decreases, as compared with the intensity distribution of the MIP image at the first iteration shown in Fig. 3(b). This leads to the left-shift of the Gaussian distribution with a higher mean in the mixture model. Consequently, a relatively low threshold is selected to segment the MIP image, as a result of oversegmentation, as illustrated in Fig. 4(b).

In this paper we propose an automatic mechanism to detect the left-shift of the Gaussian distribution with a higher mean to the lower-intensity region. Suppose that the current iteration of the algorithm execution is  $k$ . Let  $h_k^B$  be the estimated background intensity distribution at iteration  $k$  obtained with the threshold  $t_{k-1}$  calculated at the previous iteration  $k-1$ . The distribution  $h_k^B$  is given by

$$h_k^B(i) = \begin{cases} h_k(i), & \text{if } i < t_{k-1}; \\ 0, & \text{otherwise;} \end{cases} \quad (6)$$

where  $h_k$  is the observed intensity distribution of the MIP image at iteration  $k$  and  $i$  is the intensity value. Let  $h_k^G$  be the estimated Gaussian distribution with a lower mean in the mixture model and  $h_k^{GG}$  be the overall distribution of the double-Gaussian mixture model. The proposed mechanism calculates the sums of absolute difference (SAD) between  $h_k^B$  and the two distributions,  $h_k^G$  and  $h_k^{GG}$ , respectively. The differences between  $\text{SAD}(h_k^B, h_k^{GG})$  and  $\text{SAD}(h_k^B, h_k^G)$  are evaluated. If the Gaussian distribution with a higher mean is left-shifted, it is expected to have a smaller SAD value between  $h_k^B$  and  $h_k^{GG}$  than the one between  $h_k^B$  and  $h_k^G$ . This is because  $h_k^{GG}$  gives a better approximation on  $h_k^B$  when the Gaussian distribution with a higher mean is shifted to the low-intensity range. The stopping criterion of the algorithm is, therefore, to see if  $\text{SAD}(h_k^B, h_k^G) > \text{SAD}(h_k^B, h_k^{GG})$ .

For a better illustration, Fig. 5(a) shows the difference between  $\text{SAD}(h_k^B, h_k^{GG})$  and  $\text{SAD}(h_k^B, h_k^G)$  [i.e.,  $\text{SAD}(h_k^B, h_k^{GG}) - \text{SAD}(h_k^B, h_k^G)$ ], obtained throughout the algorithm execution in an experiment on the dataset presented in Fig. 4. It is observed that the SAD value difference decreases from 0.15 to  $-0.03$  as the algorithm proceeds. The difference is below 0 at the 16th iteration. This indicates the effect of the left-shift of the Gaussian distribution with a higher mean. Among the other 11 clinical datasets, similar patterns of a decreasing SAD value difference are observed, as presented in Figs. 5(b)–5(l). With these figures, the convergence of the algorithm can be shown experimentally.

According to the proposed stopping criterion, the only condition that makes the algorithm fail to converge and terminate is that the left-shift of the Gaussian distribution with a higher mean never occurs. In other words, a severe imbalance between the proportions of the vessels and the background never occurs for the MIP image. However, during the algorithm execution, more and more vessel voxels are excluded in the MIP image generation. That is, the proportion of the vessels keeps decreasing and that of the background keeps increasing. The imbalance between the two proportions only becomes more and more severe, until finally the aforsaid left-shift occurs and the algorithm terminates.

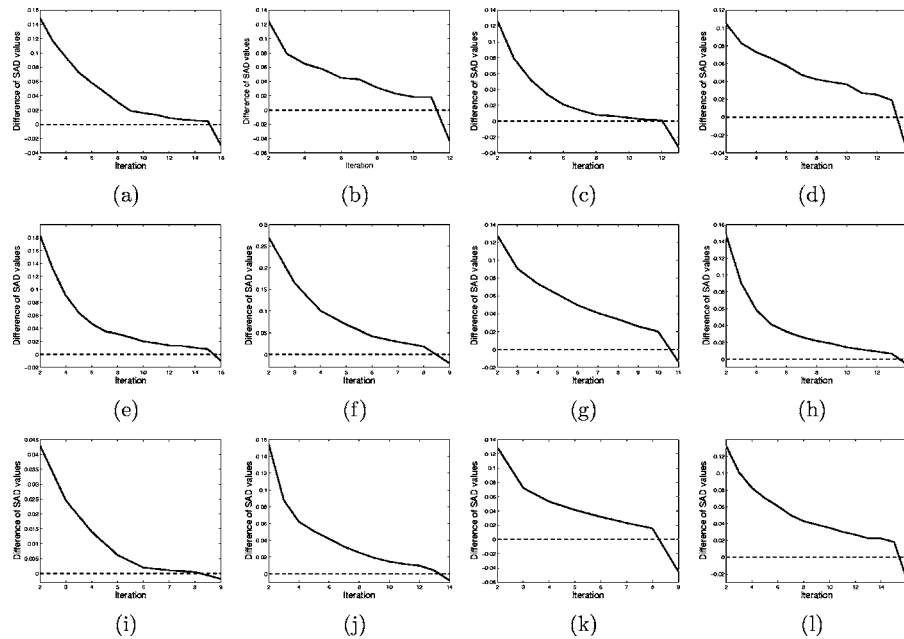


FIG. 5. The differences between SAD values obtained throughout the algorithm execution for all 12 datasets.

Once the stopping criterion is satisfied at the last iteration, the algorithm stops generating and segmenting MIP images and gives the compiled 3D vascular segmentation as the final segmentation. However, it does not imply that no vessel voxel can be found in the rest of the 3D volume, which is referred to as the volume that excluded all the segmented vessel voxels. As such, in order not to leave out any vessel voxels, the threshold selected at the second last iteration (hereafter referred as to  $\hat{t}$ ) is applied to segment the rest of the 3D volume. Note that the threshold estimated at the last iteration cannot be used because the Gaussian distribution with a higher mean has already left-shifted and then the estimated threshold can lead to oversegmentation.

One may be confused by the aforesaid step and presume that the method produces vascular segmentation that is identical to the one obtained by the global thresholding method with the threshold  $\hat{t}$ . However, if the two segmentations are compared, it is not difficult to realize that the two methods do produce different vascular segmentations. As a further justification of this proposition, it is empirically observed that, for all the 12 clinical datasets, the threshold estimated at the second last iteration  $\hat{t}$  is not the smallest threshold among the others. This implies that voxels with intensity values lower than  $\hat{t}$  are picked up and added to the 3-D vascular segmentation before the stopping criterion is satisfied. As such, it is clear that the segmentation produced by the proposed method can be different from the one obtained from the global thresholding method with the threshold  $\hat{t}$ .

### C. Extension to use multiple projection directions

As discussed in Sec. IV A, the algorithm segments the MIP images projected along one of the three principal axes in order to avoid unnecessary intensity interpolation. However, it is not clear how to decide which projection direction

should be used. Moreover, it is not feasible to use a single statistical mixture model to simultaneously approximate the intensity distributions in the MIP images along the three principal axes, due to the different proportions of the projected vascular regions in the three MIP images. As such, an empirical study has been conducted to evaluate which projection direction yields better segmentation on the 12 3D-RA datasets (see Sec. V B for more details). It is found that no single projection direction outperforms the others across all the datasets, and there is a large deviation in the quality of segmentations produced with the MIP images generated along different projection directions. Therefore, it is preferable to have a more robust algorithm that can produce vascular segmentation of high quality with reference to the sagittal, coronal, and axial (projections along the  $X$  axis,  $Y$  axis, and  $Z$  axis, respectively) MIP images.

In this paper we propose a proper extension of the above proposed technique to exploit the segmentation of MIP images projected along the three principal axes. The extension can be summarized as follows: (1) the aforementioned algorithm is separately executed with MIP images generated along the  $X$  axis,  $Y$  axis, and  $Z$  axis; and (2) the obtained three segmentations are combined under an aggregation scheme to derive the final vascular segmentation.

In this work we propose and evaluate the following aggregation schemes: (1) *union*, voxels that have been counted on any one of the three segmentations are included in the final segmentation; (2) *intersection*, only voxels that have been counted on all the three segmentations are included in the final segmentation; and (3) *winner-takes-all* (WTA), voxels that have been counted on two out of the three segmentations are included in the final segmentation. The evaluation results are given in Sec. V B. It is found that WTA aggregation scheme demonstrates higher robustness than the other

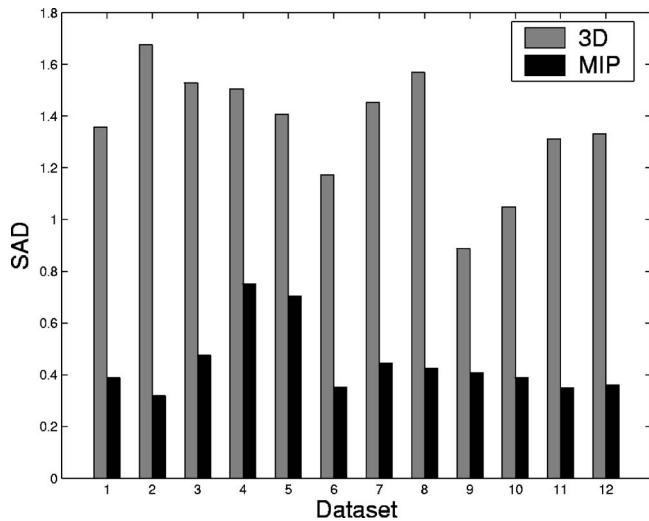


FIG. 6. The SAD values between the estimated Gaussian distribution and the observed distribution of vessels.

two schemes in the experiments on the 12 clinical datasets and produces segmentations of 3D-RA images with stable quality (see Sec. V B for more details). Furthermore, the segmentations produced under the WTA aggregation scheme exhibit a high degree of agreement with the manual segmentations.

## V. EXPERIMENTS AND DISCUSSION

The proposed algorithm has been applied on 12 clinical 3D-RA datasets acquired by a Philips Integris imager at the Department of Diagnostic Radiology and Organ Imaging, Prince of Wales Hospital, Hong Kong. The data volume is around  $100 \times 100 \times 100$  voxels with a voxel size of  $0.75 \times 0.75 \times 0.75$  mm<sup>3</sup>. The volume is cropped to exclude null-intensity regions that contain no signal at all. Furthermore, the 12 datasets were manually segmented with the help of a consultant radiologist. The manual segmentations, which were voxel-by-voxel selections, were treated as the ground truth in all experiments presented in this section.

### A. Experiments on statistical modeling

The statistical modeling of the intensity distribution of vessels in the 3D-RA images and their corresponding MIP images has been tested. The EM algorithm is used to estimate the parameters of the double-Gaussian distribution, as discussed in Sec. II. In order to compare the goodness-of-fit of the estimated Gaussian distribution with the observed distribution for the vessel class, the sum of absolute difference (SAD) is chosen to measure the similarity between the estimated Gaussian distribution and the observed distribution of vessels, which is obtained based on the manual segmentation. The value of SAD between two distributions is between 0 and 2. The SAD value is small and close to 0 if the two distributions, i.e., the estimated mixture model and the observed distribution, fit each other, while it is large and close to 2 if the distributions do not overlap.

Figure 6 plots the SAD values between the estimated

Gaussian distribution and the observed distribution of vessels for the 12 3D volumes and the corresponding MIP images. The mean and the standard deviation of the SAD values for the 3D volumes are 1.35 and 0.23, respectively, while those for the MIP images are 0.45 and 0.14, respectively. It is indicated that the statistical modeling of the intensity distribution of vessels in MIP images is more accurate than the modeling in 3D volumes (the mean of SAD values equals 0.45 vs 1.35).

### B. Justification of the extension to use multiple projection directions

In order to justify the necessity of the extension to the application of multiple MIP images, the algorithm with sagittal (projection along the  $X$  axis), coronal (projection along the  $Y$  axis), and axial (projection along the  $Z$  axis) MIP images have been separately tested on all the 12 datasets (hereafter referred as to MIP-SP- $X$ , MIP-SP- $Y$ , and MIP-SP- $Z$ , respectively). The obtained segmentations are then compared based on a similarity measure toward the ground truth (i.e., the manual segmentations). Suppose  $X$  is one of the segmentations produced by the proposed method and  $\hat{X}$  is the corresponding ground truth. The similarity between the two segmentations is measured by the Dice similarity coefficient (DSC).<sup>27</sup> DSC is defined as the ratio of twice the common vessel volume to the sum of the individual vessel volumes in the two given segmentations. It takes both the sensitivity and specificity into account in the measurement of agreement. DSC is expressed as follows:

$$DSC(X) = \frac{2 \cdot |\mathcal{V}(\hat{X}) \cap \mathcal{V}(X)|}{|\mathcal{V}(\hat{X})| + |\mathcal{V}(X)|}, \quad (7)$$

where  $\mathcal{V}(X)$  represents the set of all vessel voxels in segmentation  $X$ ,  $\cap$  denotes the intersection operator, and  $|\mathcal{V}(\cdot)|$  denotes the total number of elements in the set  $\mathcal{V}(\cdot)$ .

With the empirical approaches, it is observed that no single method (i.e., MIP-SP- $X$ , MIP-SP- $Y$ , and MIP-SP- $Z$ ) outperforms the others across all the datasets. Furthermore, a large deviation in the quality of segmentations is produced by the algorithm with MIP images in different projection directions.

Therefore, it is preferable to have an algorithm that can produce the segmentation of high quality with reference to the sagittal, coronal, and axial MIP images. This algorithm is expected to be robust, since it does not depend on a particular maximum intensity projection direction. This paper tested three aggregation methods to combine the segmentations obtained by MIP-SP- $X$ , MIP-SP- $Y$ , and MIP-SP- $Z$ . The three aggregation methods are as follows: (1) union, (2) intersection, and (3) winner takes all as mentioned in Sec. IV C. The corresponding algorithms were named MIP-MP- $\cup$ , MIP-MP- $\cap$ , and MIP-MP-WTA, respectively. Figure 7 plots the difference between the DSC values for the aforementioned three aggregation algorithms and the highest DSC values among MIP-SP- $X$ , MIP-SP- $Y$ , and MIP-SP- $Z$  across different clinical datasets. A positive difference indicates a more

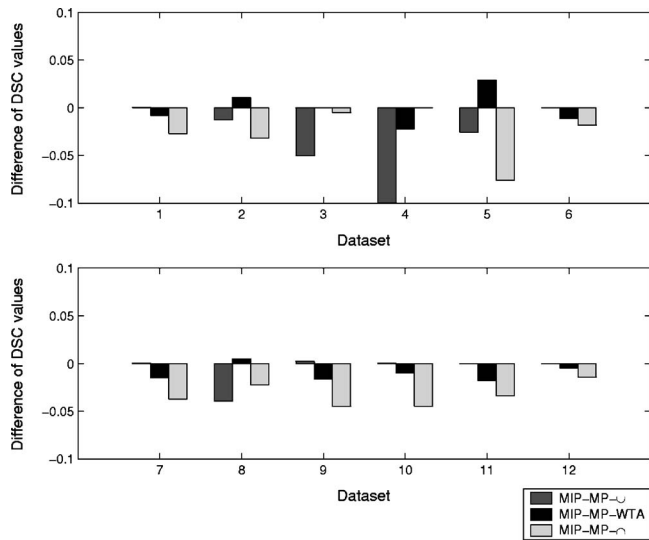


FIG. 7. The differences between DSC values for the three aggregation algorithms and the highest DSC values among MIP-SP-X, MIP-SP-Y, and MIP-SP-Z.

accurate segmentation than those produced by MIP-SP-X, MIP-SP-Y, and MIP-SP-Z. It is observed that MIP-MP-WTA can give a relatively small difference in DSC values, as opposed to MIP-MP- $\cup$  and MIP-MP- $\cap$ . As such, the results suggest that MIP-MP-WTA is a better aggregation scheme for the proposed method to be used in the clinical environment.

### C. Performance comparisons of the algorithm

In order to study the segmentation accuracy of the proposed method, auto-GT, and the new method (MIP-MP-WTA) have been applied to the 12 clinical datasets for comparison. Implementation details of the two methods are listed below.

(1) *Auto-GT*: the double-Gaussian mixture model [see Eq. (5)] is used. The parameters  $\omega_1$ ,  $\mu_1$ , and  $\sigma_1$  are initialized by calculating the proportion, the sample mean, and the standard deviation of the 99% highest posterior density (HPD) interval of the observed intensity histogram, while the other parameters  $\omega_2$ ,  $\mu_2$ , and  $\sigma_2$  are calculated from the residual histogram.

(2) *MIP-MP-WTA*: the parameters of the double-Gaussian mixture model at each iteration are initialized in the following way. At the first iteration, the parameters  $\omega_1$ ,  $\mu_1$ , and  $\sigma_1$  are initialized by calculating the proportion, the sample mean, and the standard deviation of the 90% HPD interval of the observed intensity histogram, and the other parameters  $\omega_2$ ,  $\mu_2$ , and  $\sigma_2$  are calculated from the residual histogram. In the successive iterations, the parameters estimated in the last iteration are used in the initialization of the current iteration.

Figure 8 presents the DSC values for auto-GT, MIP-MP-WTA, and the segmentation produced by the manual optimal global thresholding method (hereafter referred as to opt-GT). The manual optimal threshold is an intensity value that can

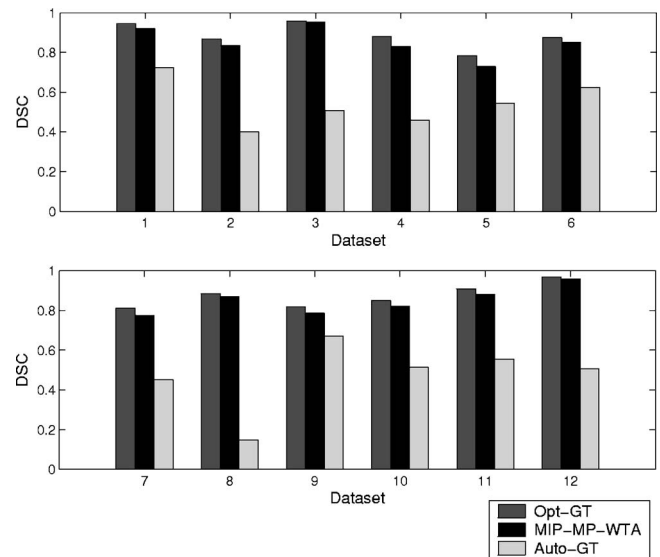


FIG. 8. The DSC values for opt-GT, auto-GT, and MIP-MP-WTA across 12 datasets.

produce segmentation with the global thresholding method in maximum agreement, measured by DSC, to the ground truth. In other words, this threshold is the best global threshold that an operator can obtain if the ground truth is known in advance. From the figure, it is indicated that the new method (MIP-MP-WTA) consistently produces segmentations with DSC values greater than 0.7. A DSC value that is greater than 0.7 indicates excellent agreement.<sup>28</sup> This implies that those segmentations are in a high degree of agreements to the ground truth, which can also be justified by the small differences in the DSC values with the opt-GT. On the contrary, auto-GT gives very low DSC values, as low as 0.1, which vary a lot across different clinical datasets.

As a further comparison, the false positive rate (FPR) is also used to evaluate the accuracy of the obtained segmentations with respect to the ground truth. FPR is defined by one minus specificity, i.e., the probability that a background voxel is classified as a vessel. Figure 9 exhibits the FPR values for opt-GT, auto-GT, and MIP-MP-WTA. It is shown that the FPR values for opt-GT and MIP-MP-WTA are consistently comparable and small. On the other hand, the FPR values for auto-GT are relatively large, which implies that the segmentations obtained via auto-GT are always oversegmented.

Figure 10 shows the regions of interests (ROI) of image slices from 3 3D-RA clinical datasets. Three rows in the figure are for individual datasets respectively. In each row, column A shows the image of the ROI, column B shows the manual segmentation (i.e., the ground truth), columns C, D, and E show the segmentations obtained by opt-GT, auto-GT, and MIP-MP-WTA, respectively. It is observed that the segmentations obtained by opt-GT and MIP-MP-WTA are very similar to manual segmentations. Among the segmentations shown in columns B, C, and E, there are discrepancies in only a few voxels. Contrarily, the segmentations obtained by

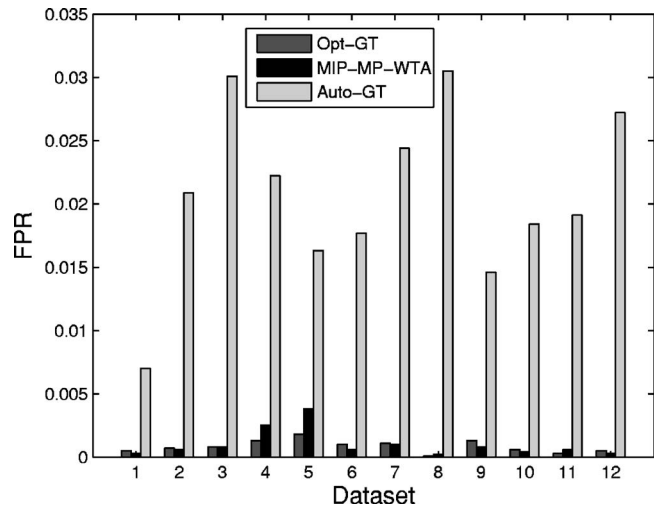


FIG. 9. The FPR values for opt-GT, auto-GT, and MIP-MP-WTA across 12 datasets.

auto-GT are less than satisfactory. The vascular segmentations include part of the dim nonvascular structures in the background, as shown in column D.

Figure 11 shows volume-rendered images of 2 3D-RA datasets. Two rows are for individual datasets, respectively. In each row, Column A shows the axial MIP image, columns B, C, and D show the volume-rendered images based on the manual segmentation, auto-GT, and MIP-MP-WTA, respectively. Volume rendering is performed by the Visualization ToolKit (VTK). It is clear from the figures that the proposed technique is capable of segmenting 3D-RA images automatically with a high degree of agreement to the manual segmentations. Although it is observed that there are some nonvas-

cular structures included in the segmentations in column D, they can be removed automatically by a connectivity filter. The segmentation of major vessels is the current radiologists' primary interest in this work and it is expected that the overall quality of the segmentations will not be affected after the application of the connectivity filter. This is because these nonvascular structures are sparse and highly isolated from the major vascular structures, as opposed to those obtained by auto-GT where the nonvascular structures are attached to the major vessels (for better illustrations, see column D in Fig. 10).

The proposed method is computationally efficient. In all the experiments presented in this section, it takes less than 20 iterations and less than 2 s to terminate for segmenting a 3D-RA image with around  $100 \times 100 \times 100$  voxels on a 2.26 GHz PC with 512 MB RAM.

### VI. CONCLUSION AND FUTURE WORK

A novel automatic segmentation technique has been presented to extract vasculature for 3D rotational angiography (3D-RA) based on maximum intensity projections (MIP). It makes use of the fact that there is a larger proportion of vessels in the MIP image as compared with the original 3D volume. This can greatly help to increase the accuracy in the parameter estimation of a finite mixture model (FMM) with the expectation maximization (EM) algorithm. The new method takes an iterative approach to segmenting 3D-RA images progressively with the segmentation of MIP images along the three principal axes. Once the results along individual axes are obtained, the results are combined using the winner-takes-all strategy. Apparently, the proposed method differs much from the 3D region growing segmentation al-

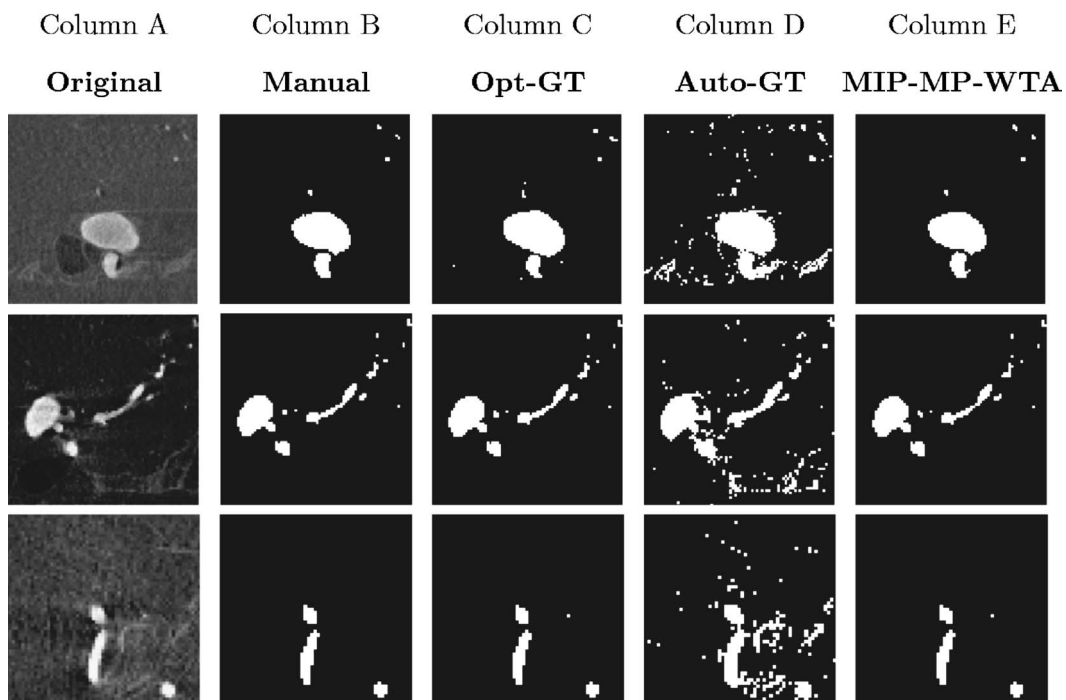


FIG. 10. Comparisons on ROI of image slices from 3 3D-RA clinical datasets, where each row is for an individual dataset.

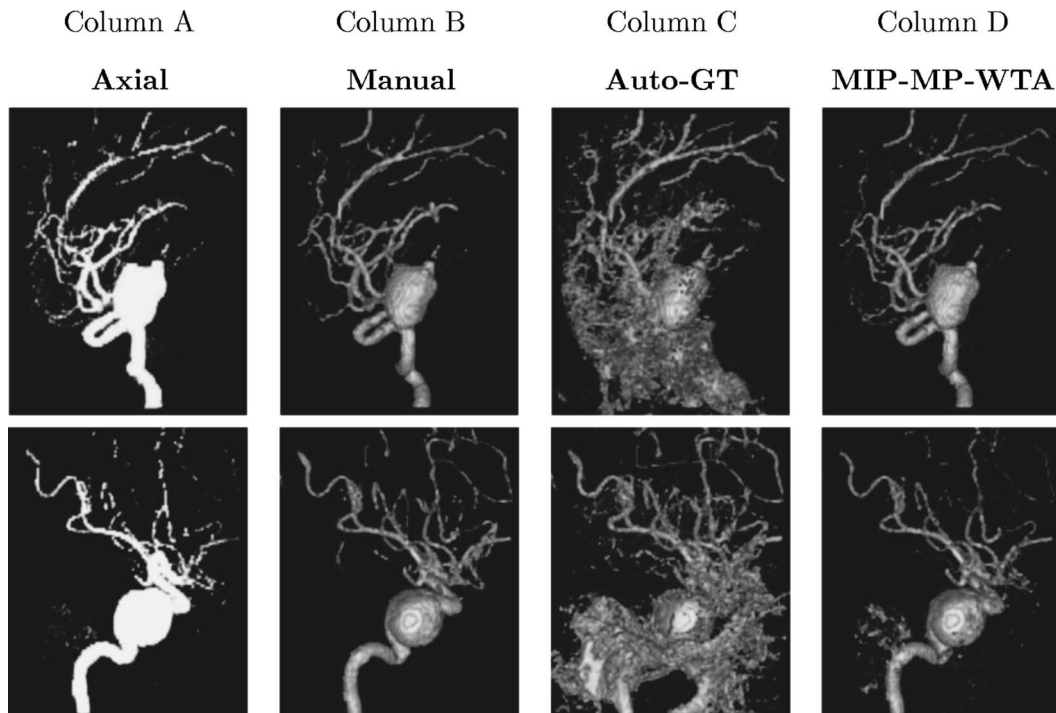


FIG. 11. Comparisons on volume-rendered images of 2 3D-RA datasets, where each row is for an individual dataset.

gorithm presented by Chapman *et al.*,<sup>6</sup> which makes use of continuity in the MIP depth  $Z$  buffer as a preprocessing step to generate seed points.

In this work, the proposed algorithm has been tested and verified on 12 clinical 3D-RA datasets. The experimental results have indicated that the novel automatic method can produce more accurate vascular segmentation than the automatic global thresholding method based on FMM and the EM algorithm. Moreover, the algorithm is capable of producing satisfactory segmentations with a very high degree of agreement to the manual segmentations. On average, the new technique is computationally efficient, and takes less than 2 s to segment a 3D-RA dataset with around  $100 \times 100 \times 100$  voxels. This makes the time-critical medical applications of the method possible.

There are several areas that are of interest for future research. A larger evaluation study with more consultant radiologists is planned to validate the algorithm over a larger set of clinical datasets. With more manual segmentations, less subjective ground truth can be obtained via the method of Warfield *et al.*<sup>29</sup> Alternatively, manual segmentations for each dataset from different radiologists can be individually used as the ground truth and the results can be evaluated together for a more objective study. Further studies on statistical properties of MIP images and performance evaluation in view of a clinically relevant task (e.g., quantification of vascular anomalies) will also be considered. Moreover, it is interesting to apply and extend the technique to modalities such as phase contrast magnetic resonance angiography (MRA) and time-of-flight MRA. Finally, the incorporation with other sophisticated segmentation techniques to refine results obtained by the proposed method is part of the future

work. For instance, the refinement via the Markov random field-based method or the model-based method can be for very small (or dim) fragmented vessels, and the refinement via the level-set method based technique can be for achieving subvoxel accuracy.

## ACKNOWLEDGMENTS

The authors are grateful to Dr. Simon Yu at the Dept. of Diagnostic Radiology and Organ Imaging, Prince of Wales Hospital, Hong Kong for his help in provision of experimental data and validation. The authors would like to acknowledge the support of the Hong Kong Research Grants Council (HK RGC) under Grant HKUST6209/02E and Grant HKUST6155/03E.

<sup>a</sup>)Electronic mail: raygan@cs.ust.hk

<sup>b</sup>)Electronic mail: cswilbur@cs.ust.hk

<sup>c</sup>)Electronic mail: achung@cs.ust.hk

<sup>1</sup>K. Krissian, G. Malandain, N. Ayache, R. Vaillant, and Y. Troussel, "Model-based detection of tubular structures in 3D images," *Comput. Vis. Image Underst.* **80**, 130–171 (2000).

<sup>2</sup>S. Aylward and E. Bullitt, "Initialization, noise, singularities, and scale in height ridge traversal for tubular object centerline extraction," *IEEE Trans. Med. Imaging* **21**, 61–75 (2002).

<sup>3</sup>W. J. Niessen, C. M. van Bommel, A. F. Frangi, M. J. A. Siers, and O. Wink, "Model-based segmentation of cardiac and vascular images," in *Proceedings of the IEEE International Symposium on Biomedical Imaging (ISBI)*, 2002, pp. 22–25.

<sup>4</sup>C. F. Westin, L. M. Lorigo, O. D. Fauger, W. E. L. Grimson, S. Dawson, A. Norbash, and R. Kikinis, "Segmentation by adaptive geodesic active contours," in *Proceedings of International Conference on Medical Image Computing and Computer-Assisted Intervention (MICCAI'00)*, Pittsburgh, Pennsylvania, October 11–14, 2000, pp. 266–275.

<sup>5</sup>L. M. Lorigo, O. D. Fauger, W. E. L. Grimson, R. Keriven, R. Kikinis, A. Nabavi, and C. F. Westin, "CURVES: Curve evolution for vessel segmentation," *Med. Image Anal.* **5**, 195–206 (2001).

- <sup>6</sup>B. Chapman, J. Stapelton, and D. Parker, "Intracranial vessel segmentation from time-of-flight MRA using pre-processing of the mip z-buffer: accuracy of the zbs algorithm," *Med. Image Anal* **8**, 113–126 (2004).
- <sup>7</sup>D. L. Wilson and J. A. Noble, "An adaptive segmentation algorithm for time-of-flight MRA data," *IEEE Trans. Med. Imaging* **18**, 938–945 (1999).
- <sup>8</sup>D. L. Wilson and J. A. Noble, "Segmentation of cerebral vessels and aneurysms from MR angiography data," in *Proceedings of International Conference on Information Processing in Medical Imaging (IPMI'97), Pourtney, Vermont, June 9-13, 1997*, pp. 423–428.
- <sup>9</sup>M. S. Hassouna, A. A. Farag, S. Hushek, and T. Moriarty, "Statistical-based approach for extracting 3D blood vessels from TOF-MRA data," in *Proceedings of International Conference on Medical Image Computing and Computer-Assisted Intervention (MICCAI'03), Montreal, Canada, November 15-18, 2003*, pp. 680–687.
- <sup>10</sup>A. C. S. Chung, J. A. Noble, and P. Summers, "Fusing speed and phase information for vascular segmentation of phase contrast MR angiograms," *Med. Image Anal* **6**, 109–128 (2002).
- <sup>11</sup>A. C. S. Chung, J. A. Noble, and P. Summers, "Vascular segmentation of phase contrast magnetic resonance angiograms based on statistical mixture modeling and local phase coherence," *IEEE Trans. Med. Imaging* **23**, 1490–1507 (2004).
- <sup>12</sup>M. S. Hassouna, C. B. Sites, A. A. Farag, S. Hushek, and T. Moriarty, "Statistical cerebrovascular segmentation for phase-contrast MRA data," in *Proceedings of International Conference on Biomedical Engineering (ICBE'02), Cairo, Egypt, December, 2002*, pp. 32–37.
- <sup>13</sup>J. Moret, R. Kemkers, J. O. de Beek, R. Koppe, E. Klotz, and M. Grass, "3D rotational angiography: Clinical value in endovascular treatment," *Med. Mundi* **42**, 8–14 (1998).
- <sup>14</sup>R. Kemkers, J. O. de Beek, H. Aerts, R. Koppe, E. Klotz, M. Grass, and J. Moret, "3D-rotational angiography: First clinical application with use of a standard philips C-arm system," in *Proceedings of the 12th International Symposium and Exhibition, Computer Assisted Radiology and Surgery (CAR'98), Tokyo, Japan, June 24-27, 1998*, pp. 182–187.
- <sup>15</sup>M. Grass, R. Koppe, E. Klotz, R. Proksa, M. H. Kuhn, H. Aerts, J. O. de Beek, and R. Kemkers, "Three-dimensional reconstruction of high contrast objects using C-arm image intensifier projection data," *Comput. Med. Imaging Graph.* **23**, 311–321 (1999).
- <sup>16</sup>Y. Troussset, R. Vaillant, L. Launay, J.-M. Obadia, N. Pivet, R. Anxionnat, and L. Licard, "A fully automated system for three-dimensional X-ray angiography," in *Proceedings of the 13th International Symposium and Exhibition, Computer Assisted Radiology and Surgery (CAR'99), Paris, France, June 23-26, 1999*, pp. 39–43.
- <sup>17</sup>E. Meijering, W. Niessen, J. Weickert, and M. Viergever, "Diffusion-enhanced visualization and quantification of vascular anomalies in three-dimensional rotational angiography: Results of an in-vitro evaluation," *Med. Image Anal* **6**, 215–233 (2002).
- <sup>18</sup>R. Gan, W. C. K. Wong, A. C. S. Chung, and S. C. H. Yu, "Statistical cerebrovascular segmentation in three-dimensional rotational angiography based on maximum intensity projections," in *Proceedings of the 18th International Congress and Exhibition, Computer Assisted Radiology and Surgery (CARS 2004), Paris, France, June 23-26, 2004*, pp. 195–200.
- <sup>19</sup>J. K. Fwu and P. M. Djurić, "EM algorithm for image segmentation initialized by a tree structure," *IEEE Trans. Image Process.* **6**, 349–352 (1997).
- <sup>20</sup>W. M. Wells, R. Kikinis, W. E. L. Grimson, and F. Jolesz, "Adaptive segmentation of MRI data," *IEEE Trans. Med. Imaging* **15**, 429–442 (1996).
- <sup>21</sup>C. Bishop, *Neural Networks for Pattern Recognition* (Clarendon, Oxford, 1995).
- <sup>22</sup>A. H. Andersen and J. E. Kirsch, "Analysis of noise in phase contrast MR imaging," *Med. Phys.* **23**, 857–869 (1996).
- <sup>23</sup>S. C. Horii and Y. Kim, *Handbook of Medical Imaging, Volume 3: Display and PACS* (SPIE—The International Society for Optical Engineering, Bellingham, WA, 2000), Vol. 3.
- <sup>24</sup>C. W. Bakal, J. E. Silberzweig, J. Cynamon, and S. Sprayregen, *Vascular and Interventional Radiology: Principles and Practice* (Thieme Medical Publishers, Inc., New York, 2002).
- <sup>25</sup>S. M. Hertz, R. A. Baum, R. S. Owen, G. A. Holland, D. R. Logan, and J. P. Carpenter, "Comparison of magnetic resonance angiography and contrast arteriography in peripheral arterial stenosis," *Am. J. Surg.* **166**, 112–116 (1993).
- <sup>26</sup>S. Napel, M. P. Marks, G. D. Rubin, M. D. Dake, C. H. McDonnell, S. M. Song, D. R. Enzmann, and R. B. Jeffrey, "CT angiography with spiral CT and maximum intensity projection," *Radiology* **185**, 607–610 (1992).
- <sup>27</sup>A. P. Zijdenbos, B. M. Dawant, R. A. Margolin, and A. C. Palmer, "Morphometric analysis of white matter lesions in MR images: Method and validation," *IEEE Trans. Med. Imaging* **13**, 716–724 (1994).
- <sup>28</sup>J. J. Bartko, "Measurement and reliability: statistical thinking considerations," *Schizophr Bull.* **17**, 483–489 (1991).
- <sup>29</sup>S. K. Warfield, K. H. Zou, and W. M. Wells III, "Validation of image segmentation and expert quality with an expectation-maximization algorithm," in *Proceedings of International Conference on Medical Image Computing and Computer-Assisted Intervention (MICCAI'02), Tokyo, Japan, September 25-28, 2002*, pp. 298–306.